A fluid lubrication analysis including negative pressure using a physically consistent particle method

Hideyo Negishi[1,3] · Masahiro Kondo[2] · Hiroaki Amakawa[1] · Shingo Obara[1] · Ryoichi Kurose[3]

Abstract

In recent years, particle methods, which are good for moving boundary problems, have become an effective approach to understand and predict flows in complex geometry, such as lubrication behaviors in rolling bearings. This study adopted a physically consistent particle method, i.e., the moving particle hydrodynamics for incompressible flows (MPH-I) method. For capturing the free surface flows in lubrication, a surface tension model was included. In order to maintain the physical consistency in the MPH-I method, the surface tension model expressed with the two density potentials, which are cohesive pressure potential (CPP) and density gradient potential (DGP), was adopted. The MPH-I method with the two-potential-based surface tension model enabled to handle negative pressure and nearly incompressible flow with very large bulk modulus. In fact, the MPH-I method could successfully reproduce fundamental pressure generation effects in the fluid film lubrication, i.e., the wedge film and squeeze film effects. Furthermore, the computed lubrication pressure agreed well with the experimental results and the classic prediction with Reynolds equation. This implies that the present numerical method was validated under the fluid film lubrication problems.

1 Introduction

Particle methods, represented by Smoothed Particle Hydrodynamics (SPH) method [1, 2] and Moving Particle Semi-implicit (MPS) method [3], are mesh-free and Lagrangian approaches, which are better at capturing moving boundary than conventional mesh-based Eulerian methods. Many studies on particle methods have been conducted, especially for free-surface flows with large deformations, multi-phase flows, fluid-rigid body coupling problems and fluid–structure coupling problems. In recent years, particle methods

have realized numerical simulations, which had been difficult using the conventional mesh-based Eulerian methods, and they are applied in various engineering field, such as nuclear engineering, civil engineering, marine engineering, mechanical engineering. [4–9].

Concerning mechanical engineering, in particular, the application of particle methods to fluid film lubrication problems has been making breakthroughs. Using the SPH method, Ji et al. [10] simulated lubricant oil behavior and revealed the flowfield in a gear box. Muto et al. [11] simulated stirred fluid flows with rotating gears and predicted the fluid resistance of the gear for a low rotational rate using the MPS method. Yuhashi et al. [12] simulated stirred fluid flows with rotating camshafts, and the torque value showed good agreement with experimental results using the MPS method. Yuhashi et al. [13] simulated oil churning in the crankcase of a reciprocating pump. They enhanced the lubrication performance of the pumps by improving the crankcase shape. Those studies are applications of the particle methods to macroscopic free surface flows in mechanical elements with complex geometry and are good examples that make full use of the advantages of the particle methods.

✉ Hideyo Negishi
negishi.hideyo@jaxa.jp

1 Japan Aerospace Exploration Agency, 2-1-1 Sengen, Tsukuba, Ibaraki 305-8505, Japan

2 National Institute of Advanced Industrial Science and Technology, Central 2, 1-1-1 Umezono, Tsukuba, Ibaraki 305-8568, Japan

3 Kyoto University, Kyoto daigaku-Katsura, Nishikyo-ku, Kyoto 615-8540, Japan

Microscopic free-surface flow simulations focused on lubricated contacts, the key physics of fluid film lubrication, have also been carried out in recent years. Kyle and Terrell [14] applied the SPH method to transient hydrodynamic lubrication in a pad bearing. They discussed the validity of the SPH method compared to the numerical solutions based on the classic Reynolds equation and the mesh-based Eulerian method. Tanaka et al. [15] simulated fluid film lubrication in line contact by using the SPH method with the Continuum Surface Force (CSF) model [16] to take the surface tension into account and an optimized particle shifting scheme [17] to enhance the robustness, and almost predicted the exit oil meniscus and pressure distribution around the contact. Paggi et al. [18] developed a fluid-rigid body coupling method based on the SPH method. They applied it to uniform and linear slider bearings, showing good agreements of the pressure distribution along the bearings with the numerical analysis based on the classic Reynolds equation. And also, a three-dimensional linear slider bearing simulation with surface roughness was demonstrated, which showed the capability of the proposed method for actual applications. Negishi et al. [19] applied the MPS method to the fluid film lubrication in line contact. They showed a good agreement of the pressure distribution around the contact with the analytical solution by the classic Reynolds equation. Yamada et al. [20] also simulated the fluid film lubrication in line contact using the MPS method with one of the multiresolution techniques, i.e., the overlapping particle technique [21]. By using larger particle spacing except for the near-contact region, the number of particles was reduced by about 60% and the computational cost by about 70% at the maximum compared to a calculation with a single resolution, predicting the analytical pressure distribution well. Those studies demonstrated that the particle methods could quantitatively predict the pressure distribution around the contact. However, in most studies, discussion was limited to positive pressure, and the negative pressure, i.e., the pressure less than the atmospheric pressure, has not been discussed sufficiently although it is crucial in the fluid film lubrication problems.

Concerning the microscopic fluid film lubrication, the surface tension and wettability play an essential role in forming the meniscus or liquid bridge around the contact. The negative pressure is induced in those meniscus or liquid bridge due to the tension when lubricated surfaces are moving apart [22]. The negative pressure significantly influences the fluid film lubrication, which can cause fluid film rapture or cavitation and determine the load and loss. Therefore, the robust and accurate prediction of the negative pressure is essential to discuss fluid film lubrication.

Predicting the negative pressure by particle methods is challenging because particles tend to be disordered or cluster due to attractive inter-particle force, and numerical simulations become unstable. That issue is classified as so-called "tensile instability," which is a common problem in both the SPH and MPS methods and can affect the convergence and accuracy of numerical simulations. Tensile instability was first discussed for the SPH method by Swegle et al. [23] and has been extensively studied by many researchers for both the SPH [17, 24–29] and MPS methods [30–33]. Up to now, a variety of techniques has been proposed to avoid tensile instability, such as the introduction of stress point [25], Lagrangian kernels [26], conservative smoothing [27], artificial repulsive forces [24, 30, 31, 33], zero-pressure limiter [30], collision model [34], particle shifting [17, 29], higher-order and consistent discretization scheme [32, 35]. Those techniques are successful in suppressing tensile instability as a means of avoiding unphysical particle behavior. Only the higher-order and consistent discretization scheme coupled with the particle shifting [17, 35] can predict the negative pressure quantitatively. However, such methods have several drawbacks: Exact linear and angular momentum conservation is not guaranteed, and empirical relaxations or parameters are involved.

In recent years, Kondo et al. [36–40] proposed a physically consistent particle method, the Moving Particle Hydrodynamics (MPH) method, which ensures overall linear and angular momentum conservation and stable calculations of particle behaviors. In the MPH method, the discretized governing equation can be fitted into the extended Lagrangian mechanics for systems with dissipation, so it satisfies the fundamental law of physics, such as the second law of the thermodynamics. This feature is called physical consistency, which guarantees that the mechanical energy monotonically decreases in a discrete system, and it does not suffer from unphysical instability without empirical relaxations [36]. Furthermore, a new physically consistent surface tension model using the combination of the two potentials, i.e., the cohesive pressure potential (CPP) and density gradient potential (DGP), was developed [40]. The promising performance of the surface tension model was demonstrated through calculating the Laplace pressure, the droplet oscillation, the wettability, the liquid bridge, and the Plateau-Rayleigh instability with using the weakly compressible version of the MPH method (MPH-WC) [38], where the explicit Euler time integration algorithm was adopted. In particular, the validation of the liquid bridge showed that the new physically consistent surface tension model could predict the negative pressure qualitatively. However, quantitative validation of the negative pressure calculation has not been carried out. Although the two-potential (CPP and DGP) surface tension model [40] was demonstrated using the MPH-WC method [38], it is expected that the model also works with the incompressible version of the MPH method (MPH-I) [36, 39] because the difference of the two, MPH-WC [38] and MPH-I [39], is only the time integration algorithm. Recently, to speed up the implicit calculation in the MPH-I method, the pressure substitution

algorithm [39] was proposed. When the explicit Euler time integration is adopted, the time step width will be restricted very small because of the small length scale and the high viscosity in the lubrication problems. Therefore, it is better to adopt the MPH-I method [39] for the lubrication calculation.

In this study, the physically consistent MPH method [36–40] with the two-potential (CPP and DGP) surface tension model [40] is applied to the fundamental fluid film lubrication problems. To cope with the small length scale and the high viscosity in the lubrication problems, the MPH-I method with the pressure substitution implicit algorithm [39] is adopted, and the Crank–Nicolson time integration method is further introduced. To validate the present numerical method including negative pressure calculation, the problems with respect to the wedge film and squeeze film effects, which are the fundamental pressure generation mechanisms in the fluid film lubrication and occur in any kind of bearings in industrial applications, are calculated in two-dimensional space. First, the wedge film in a line contact is calculated, and the computed pressure distribution is compared with the experimental result [41, 42]. Then, the parallel-surface squeeze film of infinite width is calculated, and the computed pressure history and distributions are compared with the analytical solutions using the classic Reynolds equation [43–45].

2 Numerical method

2.1 Governing equation [36, 37, 39, 40]

In this study, governing equations are the incompressible Navier–Stokes equation

$$\rho_0 \frac{D\mathbf{u}}{Dt} = -\nabla\Psi + \mu\nabla^2\mathbf{u} + \rho_0\mathbf{g} + \mathbf{f}_s \tag{1}$$

and the equation of pressure,

$$\Psi = -\lambda\nabla\cdot\mathbf{u} + \kappa\frac{\rho - \rho_0}{\rho_0}, \tag{2}$$

where ρ_0, ρ, $\mathbf{u}$, t, Ψ, μ, $\mathbf{g}$, $\mathbf{f}_s$, λ and κ are reference density, density, velocity, time, pressure, shear viscosity, gravity, bulk force with respect to surface tension, bulk viscosity, and bulk modulus, respectively. The first term on the right-hand side of Eq. (1) is the pressure, the second term is the shear viscosity, the third is gravity, and the fourth is the surface tension. In Eq. (2), the first term is the bulk viscosity, and the second is the bulk modulus. The MPH method ensures the incompressible condition by using large values for bulk viscosity λ and bulk modulus κ [36].

2.2 Discretization [37, 39, 40]

In the MPH method, the governing equations are discretized by particle interaction models based on effective radius and weight functions in the same way as in the SPH and MPS methods. The weight function used for discretizing the pressure and shear viscosity terms is as follows:

$$w_{ij} = w(|\mathbf{r}_{ij}|)$$

$$w(r) = \begin{cases} \frac{1}{S}\frac{1}{h^d}\left(1 - \frac{r}{h}\right)^2 & (r \le h) \\ 0 & (r > h) \end{cases}, \tag{3}$$

$$S = \frac{1}{\Delta V}\int_{r<h}\frac{1}{h^d}\left(1 - \frac{r}{h}\right)^2 dv$$

where $\mathbf{r}_{ij}$ is the relative position vector from particle i to j, r is the absolute value of $\mathbf{r}_{ij}$, h is the effective radius, d is the space dimension, and ΔV is the volume of a single particle region, which is a constant given by using the initial particle spacing l_0 as

$$\Delta V = l_0^d. \tag{4}$$

By using the particle interaction models in the MPH method and the continuity equation [36, 37, 39], the governing equations (Eqs. 1 and 2) are discretized as

$$m\frac{d\mathbf{u}_i}{dt} = \sum_{j\neq i}(\Psi_j + \Psi_i)\mathbf{e}_{ij}w_{ij}^{p\prime}\Delta V$$

$$- 2\mu(d+2)\sum_{j\neq i}\left(\frac{\mathbf{u}_{ij}}{|\mathbf{r}_{ij}|}\cdot\mathbf{e}_{ij}\right)\mathbf{e}_{ij}w_{ij}^{v\prime}\Delta V + m\mathbf{g} + \mathbf{F}_i^s \tag{5}$$

and

$$\Psi_i = \lambda\sum_{j\neq i}\left(\mathbf{u}_{ij}\cdot\mathbf{e}_{ij}\right)w_{ij}^{p\prime} + \kappa(n_i^p - n_0^p), \tag{6}$$

respectively, where m is the mass of a single particle ($= \rho_0\Delta V$); $\mathbf{F}_i^s$ is the surface tension force, which is explained in detail in the next sub-section; the vector $\mathbf{u}_{ij}$ in Eqs. (5) and (6) is the relative velocity from particle i to j; and the vector $\mathbf{e}_{ij}$ is the unit vector from particle i to j, which is given as

$$\mathbf{e}_{ij} = \frac{\mathbf{r}_{ij}}{|\mathbf{r}_{ij}|}. \tag{7}$$

The differential of the weight function w_{ij}' is represented by

$$w_{ij}' = w'(|\mathbf{r}_{ij}|)$$

$$w'(r) = \frac{\partial w(r)}{\partial r}. \tag{8}$$

Here, it should be noted that the differential of the weight function has a negative value. Also, the superscripts of v and p for the weight function mean the variables for the viscous and pressure terms use different effective radii h_v and h_p. The parameter n_i^p is a particle number density defined as

$$n_i^p = \sum_{j \neq i} w_{ij}^p, \tag{9}$$

and n_0^p is the reference value, calculated with a uniform particle distribution at the initial condition. Although the detailed explanation is skipped here, it is confirmed that the discretized Eqs. (5) and (6) can properly calculate the pressure and velocity [36, 37].

2.3 Surface tension force and wettability [40]

Based on the cohesive pressure potential (CPP) and density gradient potential (DGP), the surface tension force $\mathbf{F_i^s}$ is given as

$$\begin{aligned}
\mathbf{F}_i^s =& a \sum_{j \neq i} \left((n_j^a - n_0^a) + (n_i^a - n_0^a) \right) \mathbf{e}_{ij} w_{ij}^{a\prime} \Delta A \\
& - a K^2 h_s \sum_{j \neq i} (\boldsymbol{\chi}_j - \boldsymbol{\chi}_i) w_{ij}^g \Delta A \\
& - a K^2 h_s \sum_{j \neq i} \left((\boldsymbol{\chi}_j - \boldsymbol{\chi}_i) \cdot \mathbf{r}_{ij} \right) \mathbf{e}_{ij} w_{ij}^{g\prime} \Delta A,
\end{aligned} \tag{10}$$

where a is the coefficient that determines the magnitude of the surface tension, K is the parameter to control the balance of the two potentials, and h_s is the effective radius for the surface tension force, respectively. The constant ΔA is the area of a single particle defined as

$$\Delta A = \Delta V / l_0 = l_0^{d-1}. \tag{11}$$

The first term on the right side of Eq. (10) is the component of the surface tension force based on the CPP, which is turned on only when $n_i^a - n_0^a < 0$. Here, n_i^a is the particle number density for the CPP, which is different from n_i^p, and given as

$$n_i^a = \sum_{j \neq i} w_{ij}^a, \tag{12}$$

where w_{ij}^a is another weight function for the CPP defined as

$$\begin{aligned}
& w_{ij}^a = w_a(|\mathbf{r}_{ij}|) \\
& w_a(r) = \begin{cases} \frac{1}{S_a} \frac{1}{h_s^d} \frac{r}{h_s} \left(1 - \frac{r}{h_s} \right)^2 & (r \leq h_s) \\ 0 & (r > h_s) \end{cases}, \\
& S_a = \frac{1}{\Delta V} \int_{r < h_s} \frac{1}{h_s^d} \frac{r}{h_s} \left(1 - \frac{r}{h_s} \right)^2 dv
\end{aligned} \tag{13}$$

and w_{ij}^a' is the differential of w_{ij}^a. Because of the low particle number density in the vicinity of the fluid interface, the CPP force is negative, and it gives long-range attractive and short-range repulsive force based on w_{ij}^a when $n_i^a - n_0^a < 0$ so that the tensile force due to the negative pressure can be calculated without tensile instability [24]. The second and third terms on the right side of Eq. (10) are the components of the surface tension force based on the DGP. Vector $\boldsymbol{\chi}$ is an eccentric vector defined as

$$\boldsymbol{\chi}_i = h_s \sum_{j \neq i} \mathbf{r}_{ij} w_{ij}^g, \tag{14}$$

where w_{ij}^g is another weight function for the DGP given as

$$\begin{aligned}
& w_{ij}^g = w_g(|\mathbf{r}_{ij}|) \\
& w_g(r) = \begin{cases} \frac{1}{S_g} \frac{1}{h_s^d} \left(1 - \frac{r}{h_s} \right)^2 & (r \leq h_s) \\ 0 & (r > h_s) \end{cases}, \\
& S_g = \frac{1}{\Delta V} \frac{1}{d} \int_{r < h_s} r^2 \frac{1}{h_s^d} \left(1 - \frac{r}{h_s} \right)^2 dv
\end{aligned} \tag{15}$$

and w_{ij}^g' is the differential of w_{ij}^g.

In the proposed surface tension model, the DGP force is designed to cancel the perpendicular force on the fluid interface by the CPP. According to the previous study [40], the coefficient K is numerically calculated as $K \approx 0.351$ in 2D, and $K \approx 0.327$ in 3D, respectively. In addition, it is reported that the coefficient K is a dimensionless parameter determined by the shape of the weight functions and is independent from the effective radius h_s and the particle spacing l_0 [40].

The coefficient a is related to the surface tension coefficient σ estimating the surface energy, which is the potential energy per unit surface and is equivalent to σ as follows:

$$\sigma = \frac{a h_s}{l_0} I_N + \frac{a K^2 h_s}{l_0} I_X, \tag{16}$$

where I_N and I_X are calculated numerically and are $I_N \approx 0.02468$ and $I_{\mathbf{X}} \approx 0.2261$ in 2D, and $I_N \approx 0.02142$ and $I_{\mathbf{X}} \approx 0.2339$ in 3D, respectively [40]. With these values and Eq. (16), the coefficient a is calculated by a desired surface tension coefficient σ.

In this study, the solid wall is represented by wall particles, whose position and velocity are specified. The wettability is modeled by modifying the weight function for different types of particle pairs. Specifically, the weight functions of the CPP and DGP for the wall-fluid particle pairs are modified by

multiplying the interaction ratio α as

$$\begin{aligned} w_{ij}^a &= \alpha w_a(r_{ij}) \\ w_{ij}^g &= \alpha w_g(r_{ij}) \end{aligned} \text{ (Particles } i \text{ and } j \text{ are in different phases.).}$$

(17)

Here, the interaction ratio α can be related to the contact angle θ based on Young's relation, the potential energy, and the surface energy as follows [40]:

$$1 = \cos\theta + 2(1 - \alpha)^2.$$

(18)

Given the desired contact angle θ, the interaction ratio α can be calculated via Eq. (18).

In the two-potential (CPP and DGP) surface tension model employed in this study, the surface tension is modeled as the tension tangential to the free surface. The validity of the two-potential surface tension model was presented in our previous study [40] via the Laplace pressure calculation, droplet oscillation calculation, contact angle calculation, liquid bridge calculation and Plateau-Rayleigh instability calculation. Furthermore, it was revealed that the two-potential surface tension model has an ability to calculate the negative pressure, which is essential for meniscus forming, as well as the surface tension [40].

2.4 Physical consistency [36, 37, 40]

In the MPH method, the discretized governing equations (Eqs. 5, 6, and 10) are fitted into the analytical mechanical framework for the system with dissipation [46], in which the mechanical energy monotonically decreases following the second law of the thermodynamics. This feature is termed "physical consistency" and is useful to carry out particle simulations free from instability like particle scattering along with unphysical mechanical energy increase. Specifically, the extended Lagrangian equation for the system with dissipation

$$\frac{d}{dt}\left(\frac{\partial L}{\partial \mathbf{u}_i}\right) - \left(\frac{\partial L}{\partial \mathbf{x}_i}\right) + \left(\frac{\partial D}{\partial \mathbf{u}_i}\right) = \mathbf{0}$$

(19)

is applied, where L and D are Lagrangian and Rayleigh dissipation functions, respectively. The Lagrangian is defined as

$$L = T - U,$$

(20)

where T and U are the kinetic energy and potential energy of the system given as

$$T = \sum_i \frac{1}{2}m|\mathbf{u}_i|^2$$

(21)

$$U = -\sum_i m\mathbf{g}\cdot\mathbf{x}_i + \sum_i \frac{\kappa}{2}\left(n_i^p - n_0^p\right)^2 \Delta V$$
$$+ a\left(\sum_i \frac{1}{2}\left(n_i^a - n_0^a\right)^2 + \sum_i \frac{K^2}{2}|\mathbf{\chi}_i|^2\right)\Delta A.$$

(22)

The Rayleigh dissipation function is given as

$$D = \sum_i \left[\frac{\lambda}{2}\left(\sum_j (\mathbf{u}_{ij}\cdot\mathbf{e}_{ij})w_{ij}^{p'}\right)^2 + \sum_j \frac{\mu(d+2)}{2}(\mathbf{u}_{ij}\cdot\mathbf{e}_{ij})^2 w_{ij}^{v'}\right]\Delta V.$$

(23)

As a result, substituting the kinetic energy T, potential energy U, and Rayleigh dissipation function D into the Lagrangian equation (Eq. 19) leads to the discretized governing equations (Eqs. 5 and 6).

In addition to the physical consistency, the discretized governing equations (Eqs. 5 and 6) guarantee linear and angular momentum conservation. The conservative pressure gradient model is employed in the first term on the right-hand side of Eq. (5), which ensures the law of action and reaction between particles leading to linear momentum conservation [7, 47]. The pairwise damping viscous term model is applied to the second term on the right-hand side of Eq. (5), which satisfies the angular momentum conservation [37, 48]. To avoid tensile instability [24], the second term on the right side of Eq. (6) is ignored by setting κ of zero when $n_i^p - n_0^p < 0$.

The physical consistency, which is the main feature of the MPH method, is the key factor for successfully simulating the fluid lubrication problems addressed in this study. If the physical consistency is not satisfied, in general, unphysical particle behavior and unphysical mechanical energy increase may take place and result in numerical instability. In fact, tuning the artificial relaxation parameters was often needed for suppressing the instability in conventional particle methods [36]. In particular, when the potential-based surface tension model is adopted as in this study, such unphysical behaviors can deteriorate the accuracy and stability of simulation [40]. The technical challenges for simulating the fluid lubrication problems by using particle methods are (1) surface tension and wettability calculation, (2) tensile instability, and (3) stable and accurate pressure calculation. In order to handle these issues, the physical consistency is indispensable.

2.5 Time integration [39]

For the time integration of the discretized governing equations (Eqs. 5 and 6), the MPH-I method with the pressure substituting implicit solver [39] was employed to avoid the

restriction of the time step width due to the small length scale and high viscosity that characterize the fluid film lubrication.

Canceling the pressure by substituting the discretized equation of pressure (Eq. 6) into the discretized Navier–Stokes equation (Eq. 5), the velocity $\mathbf{u}_i$ is implicitly calculated as

$$
\begin{aligned}
m\frac{\mathbf{u}_i^{k+1} - \mathbf{u}_i^k}{\Delta t} \\
= -2\mu(d+2)\sum_{j\neq i}\left(\frac{\mathbf{u}_j^{k+1} - \mathbf{u}_i^{k+1}}{|\mathbf{r}_{ij}|} \cdot \mathbf{e}_{ij}\right)\mathbf{e}_{ij}w_{ij}^{v\prime}\Delta V \\
+\lambda\sum_{j\neq i}\left(\sum_{n\neq j}\left(\mathbf{u}_n^{k+1} - \mathbf{u}_j^{k+1}\right)\cdot\mathbf{e}_{jn}w_{jn}^{p\prime} + \sum_{m\neq i}\left(\mathbf{u}_m^{k+1} - \mathbf{u}_i^{k+1}\right)\cdot\mathbf{e}_{im}w_{im}^{p\prime}\right)\mathbf{e}_{ij}w_{ij}^{p\prime}\Delta V \\
+\kappa\sum_{j\neq i}\left(\left(n_j^p - n_0^p\right) + \left(n_i^p - n_0^p\right)\right)\mathbf{e}_{ij}w_{ij}^{p\prime}\Delta V \\
+\mathbf{F}_i^s + m\mathbf{g},
\end{aligned}
\tag{24}
$$

where upper index k indicates the time steps, and Δt is the time step width. The particle number densities $n_i{}^p$, $n_j{}^p$, and the surface tension force $\mathbf{F}_i{}^s$ are calculated explicitly. Equation (24) is a large linear system with a positive definite symmetric coefficient matrix. In this study, the Crank–Nicolson method was applied to Eq. (24), and the following system

$$
\begin{aligned}
m\frac{\mathbf{u}_i^{k+1} - \mathbf{u}_i^k}{\Delta t} = \beta\Bigg\{ -2\mu(d+2)\sum_{j\neq i}\left(\frac{\mathbf{u}_j^{k+1} - \mathbf{u}_i^{k+1}}{|\mathbf{r}_{ij}|} \cdot \mathbf{e}_{ij}\right)\mathbf{e}_{ij}w_{ij}^{v\prime}\Delta V \\
+\lambda\sum_{j\neq i}\left(\sum_{n\neq j}\left(\mathbf{u}_n^{k+1} - \mathbf{u}_j^{k+1}\right)\cdot\mathbf{e}_{jn}w_{jn}^{p\prime} + \sum_{m\neq i}\left(\mathbf{u}_m^{k+1} - \mathbf{u}_i^{k+1}\right)\cdot\mathbf{e}_{im}w_{im}^{p\prime}\right)\mathbf{e}_{ij}w_{ij}^{p\prime}\Delta V \Bigg\} \\
+(1-\beta)\Bigg\{ -2\mu(d+2)\sum_{j\neq i}\left(\frac{\mathbf{u}_j^k - \mathbf{u}_i^k}{|\mathbf{r}_{ij}|} \cdot \mathbf{e}_{ij}\right)\mathbf{e}_{ij}w_{ij}^{v\prime}\Delta V \\
+\lambda\sum_{j\neq i}\left(\sum_{n\neq j}\left(\mathbf{u}_n^k - \mathbf{u}_j^k\right)\cdot\mathbf{e}_{jn}w_{jn}^{p\prime} + \sum_{m\neq i}\left(\mathbf{u}_m^k - \mathbf{u}_i^k\right)\cdot\mathbf{e}_{im}w_{im}^{p\prime}\right)\mathbf{e}_{ij}w_{ij}^{p\prime}\Delta V \Bigg\} \\
+\kappa\sum_{j\neq i}\left(\left(n_j^p - n_0^p\right) + \left(n_i^p - n_0^p\right)\right)\mathbf{e}_{ij}w_{ij}^{p\prime}\Delta V \\
+\mathbf{F}_i^s + m\mathbf{g},
\end{aligned}
\tag{25}
$$

is calculated with β of 0.5 by using the conjugate gradient (CG) method. The library of iterative solvers for the linear systems (Lis) library [49, 50] is used as the matrix solver.

After getting the velocity $\mathbf{u}_i{}^{k+1}$, the position is updated as

$$
\mathbf{r}_i^{k+1} = \mathbf{r}_i^k + \mathbf{u}_i^{k+1}\Delta t.
\tag{26}
$$

2.6 Virial pressure evaluation [36, 37, 40]

The pressure in a physically consistent system, which satisfies the momentum conservation law, can be calculated via the interaction forces based on the virial theorem [51]. The calculated pressure based on the virial theorem is termed "virial pressure" for the single particle region, which is given as

$$
p_i = \frac{1}{\Delta V}\frac{1}{d}\sum_{j\neq i}\left(\mathbf{F}_{i\to j}^{\Psi} + \mathbf{F}_{i\to j}^v + \mathbf{F}_{i\to j}^{CPP} + \mathbf{F}_{i\to j}^{DGP}\right)\cdot\mathbf{r}_{ij}.
\tag{27}
$$

Here, the interaction force from particle i is expressed with regard to the pressure Ψ term (Eq. 5) as

$$
\mathbf{F}_{i\to j}^{\Psi} = -\Psi_i\mathbf{e}_{ij}w_{ij}^{p\prime}\Delta V,
\tag{28}
$$

the shear viscosity term (Eq. 5) as

$$
\mathbf{F}_{i\to j}^v = -\mu(d+2)\left(\frac{\mathbf{u}_{ij}}{|\mathbf{r}_{ij}|}\cdot\mathbf{e}_{ij}\right)\mathbf{e}_{ij}w_{ij}^{v\prime}\Delta V,
\tag{29}
$$

the CPP term (Eq. 10) as

$$
\mathbf{F}_{i\to j}^{CPP} = -a\left(n_i^a - n_0^a\right)\mathbf{e}_{ij}w_{ij}^{a\prime}\Delta A,
\tag{30}
$$

the DGP term (Eq. (10)) as

$$
\mathbf{F}_{i\to j}^{DGP} = -aK^2 h_s\boldsymbol{\chi}_i w_{ij}^g\Delta A - aK^2 h_s\left(\boldsymbol{\chi}_i\cdot\mathbf{r}_{ij}\right)\mathbf{e}_{ij}w_{ij}^{g\prime}\Delta A,
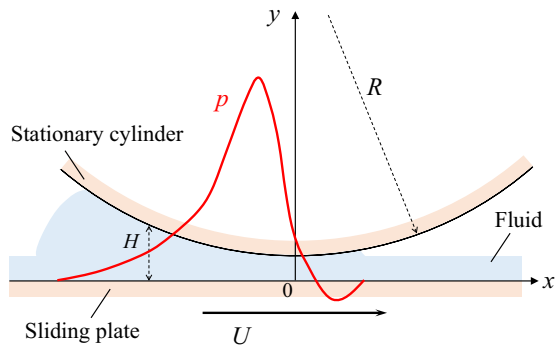\tag{31}
$$

respectively.

Fig. 1 Schematic of wedge film calculation

3 Results and discussion

3.1 Wedge film calculation

The wedge film in a line contact was calculated to validate the capability of the employed method for predicting a steady-state pressure distribution in the film. The calculation with and without the surface tension model was carried out for comparison. The computed results were compared with the result of the corresponding experiment by Floberg [41]. The wedge film is the fluid film in a converging flow passage between two geometries with a relative motion, resulting in pressure in the film, which is called the "wedge film effect"; the wedge film effect is one of the most important pressure generation mechanisms in the fluid film lubrication [43, 44].

The schematic of the wedge film calculation is illustrated in Fig. 1. The wedge film is formed between a stationary cylinder and a sliding plate with a velocity U in the horizontal direction. The flow passage has a convergent-divergent geometry around the contact, in which the positive and negative pressures are supposed to be generated. The calculation condition is shown in Table 1, where the mesh-based numerical study conducted by Bruyere et al. [42] was referred. In the calculation, the two different particle spacings of $l_0 = 5.0 \times 10^{-5}$ m and 1.0×10^{-4} m were applied to evaluate the influence of the particle resolution. The effective radii h_v and h_p for the viscous and pressure terms were both set to $3.1 l_0$, whereas the one for the surface tension model h_s was set to $3.5 l_0$. The coefficient a in the surface tension model and the interaction ratio α in the wettability model were set as in Eqs. (16) and (18). The Reynolds number Re based on the minimum film thickness at the contact H_0 and sliding velocity U is 0.391.

The computational model of the wedge film calculation at the initial state is shown in Fig. 2. The cylinder and sliding plate were modeled by wall particles, and four layers of the wall particle were given for each object. The no-slip condition was specified for the wall particles by setting a zero velocity for the cylinder and the sliding velocity U of 0.131 m/s for

Table 1 Calculation conditions for wedge film calculation

| Parameters	Base case	Coarse case
Radius of cylinder R (m)	0.05	
Minimum film thickness H_0 (m)	4.0×10^{-4}	
Initial film thickness H_{init} (m)	8.0×10^{-4}	
Sliding velocity U (m/s)	0.131	
Fluid density ρ (kg/m^3)	850	
Viscosity μ (Pa s)	0.114	
Bulk viscosity λ (Pa s)	1.0	2.0
Bulk modulus κ (Pa)	1.0×10^5	1.0×10^5
Surface tension σ (N/m)	0.032	
Coefficient a (N/m)	0.174	
Coefficient K (–)	0.351	
Contact angle θ (deg)	60	
Interaction ratio α (–)	0.5	
Gravity g (m/s^2)	9.8	
Particle spacing l_0 (m)	5.0×10^{-5}	1.0×10^{-4}
Effective radius (viscosity) h_v (m)	1.55×10^{-4}	3.1×10^{-4}
Effective radius (pressure) h_p (m)	1.55×10^{-4}	3.1×10^{-4}
Effective radius (surface tension) h_s (m)	1.75×10^{-4}	3.5×10^{-4}
Time step width Δt (s)	1.0×10^{-5}	2.0×10^{-5}
Reynolds number Re (–)	0.391	
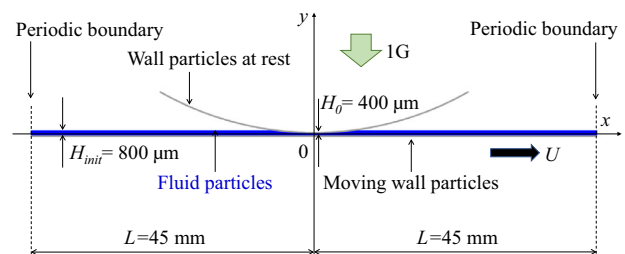
Fig. 2 Computational model of wedge film calculation

the sliding plate. The fluid film was modeled by the fluid particle, and the initial film thickness was given as $H_{\text{init}} = 8.0 \times 10^{-4}$ m. The periodic boundary condition was imposed on both sides of the boundary horizontally. The gravity was given in the vertical direction.

The shape of the wedge film for the base case ($l_0 = 5.0 \times 10^{-5}$ m) is shown in Fig. 3. The difference in shape can be seen between the cases with and without the surface tension model. In the case with the surface tension model, the meniscus is formed in both the inlet and outlet regions of the contact. In particular, the flow passage downstream of the contact is filled with the fluid film at a certain distance from the contact. In contrast, in the case without the surface tension model, the flow passage is not filled with the fluid

(a) Without surface tension

(b) With surface tension
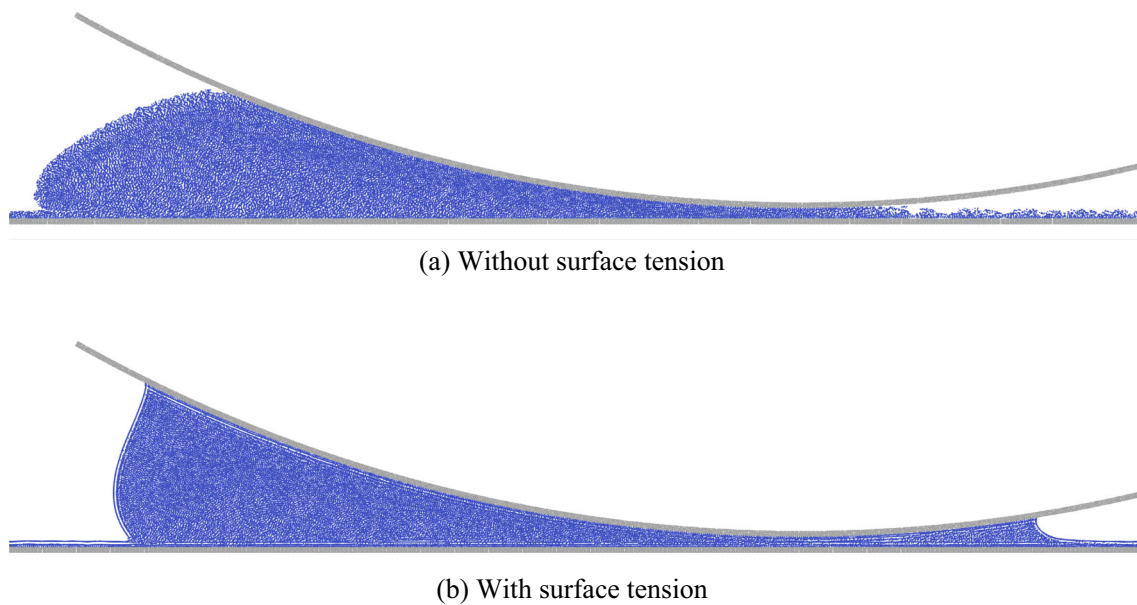
Fig. 3 Shape of wedge film calculated with $l_0 = 5.0 \times 10^{-5}$ m. **a** Without surface tension and **b** With surface tension

film, and the thickness of the film is less than the minimum gap at the contact.

The pressure distribution in the wedge film for the base case ($l_0 = 5.0 \times 10^{-5}$ m) is shown in Fig. 4. In both cases, with and without the surface tension model, the positive pressure is generated in the upstream region of the contact due to the wedge film effect. In contrast, the negative pressure can be observed downstream of the contact only in the case with the surface tension model, in which the tensile is imposed by the divergent flow passage, the sliding velocity, and the wettability in the exit meniscus. It should be noted that the simulation with respect to meniscus formation requires the negative pressure prediction. The computed result demonstrates that the two-potential surface tension model could capture the negative pressure as well as the surface tension effect. Besides, in Fig. 4b, the negative pressure is shown not only in the downstream region but also on the surface of the fluid. This is because the virial pressure (Eq. 27) on the surface turns negative with reflecting the tangential tension force coming from the two-potential surface tension model [40].

The comparison of pressure distribution in the wedge film against the experimental result [41] is shown in Fig. 5. The computed pressure in Fig. 5 was evaluated by space averaging the virial pressure (Eq. 27) in control volumes with the length of $3.1l_0$ between the cylinder and sliding plate along with 0.1 s time averaging. For comparison, the result of the coarse case with the larger particle spacing $l_0 = 1.0 \times 10^{-4}$ m is also plotted. The results show that the case with the surface tension model predicts well the entire pressure

profile, including the negative pressure regardless of the particle spacing. In contrast, the case without the surface tension model slightly overpredicts the peak of the positive pressure and fails to predict the negative pressure. As a result, it is confirmed that the wedge film effect can be predicted quantitatively by the MPH-I method with the two-potential (CPP and DGP) surface tension model.

3.2 Squeeze film calculation

The parallel-surface squeeze film of infinite width [43] was calculated to validate the employed method's capability for predicting unsteady pressure development in the film. The calculation with and without the surface tension model was carried out for comparison. The computed results were compared with an analytical solution obtained by the classic Reynolds equation. The squeeze film is the fluid film between two objects with a relative motion in a direction normal to their surfaces [43–45], resulting in pressure in the film, which is called the "squeeze film effect"; the squeeze film is the other of the most important pressure generation mechanisms in the fluid film lubrication. For example, as for rolling element bearings under varying external load, the squeeze film is formed between inner or outer races and balls, and the film thickness fluctuates in time because of the fluid-rigid body and fluid–structure interactions between them via the film itself.

The schematic of the squeeze film calculation is illustrated in Fig. 6. The squeeze film is formed between a stationary
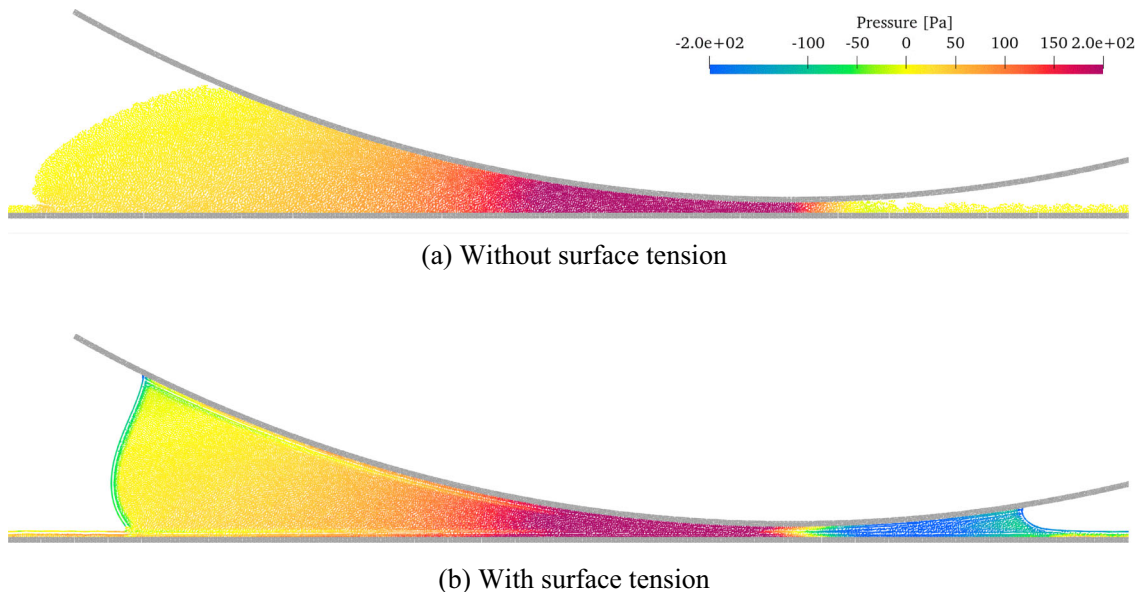
(a) Without surface tension

(b) With surface tension

Fig. 4 Pressure distribution in wedge film calculated with $l_0 = 5.0 \times 10^{-5}$ m. **a** Without surface tension and **b** With surface tension
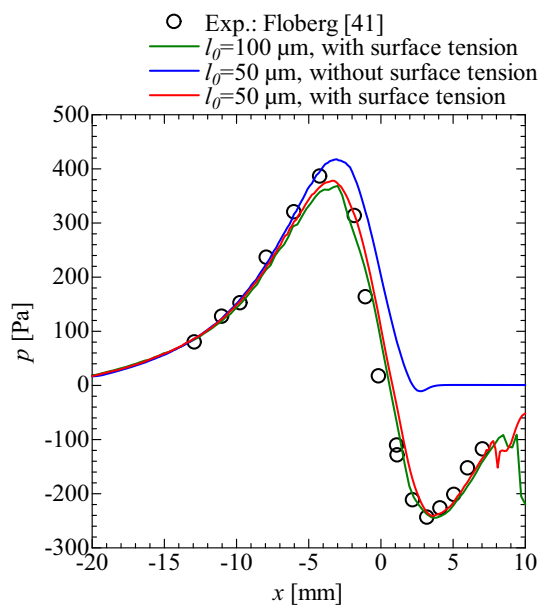

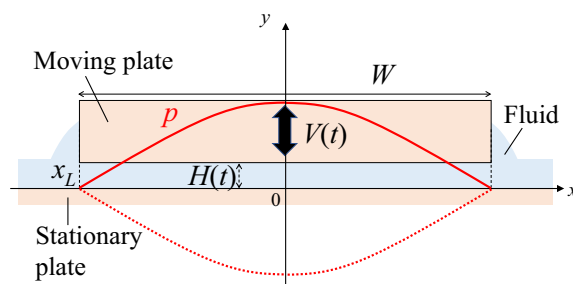**Fig. 5** Comparison of pressure distribution in wedge film against experimental result [41]

Fig. 6 Schematic of squeeze film calculation
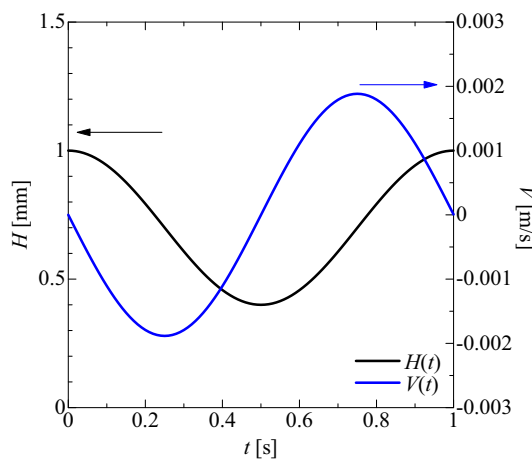
Fig. 7 Considered time history of film thickness and squeeze velocity

plate and a moving plate with a sinusoidal motion in the vertical direction, which is defined as

$$H(t) = H_0 + A[\cos(2\pi f t) - 1]$$
$$V(t) = -2\pi f A \sin(2\pi f t),$$
$$(32)$$

where H_0 is the initial film thickness, and A and f are the amplitude and frequency of the sinusoidal motion, respectively. The sinusoidal oscillation motion represents a typical behavior of the squeeze film in actual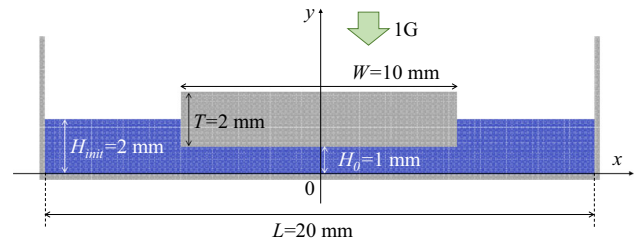 bearings. Figure 7 depicts the time history of the film thickness $H(t)$ and squeeze velocity $V(t)$ (Eq. 32) as functions of time. In the positive

Table 2 Calculation conditions for squeeze film calculation

Parameters	Base case	Coarse case
Width of moving plate W (m)	0.01	
Height of moving plate T (m)	0.002	
Initial film thickness H_0 (m)	0.001	
Initial oil height H_{init} (m)	0.002	
Amplitude of plate motion A (m)	3.0×10^{-4}	
Frequency of plate motion f (Hz)	1.0	
Fluid density ρ (kg/m^3)	850	
Viscosity μ (Pa s)	0.114	
Bulk viscosity λ (Pa s)	2.0	3.0
Bulk modulus κ (Pa)	1.0×10^6	1.0×10^6
Surface tension σ (N/m)	0.032	
Coefficient a (N/m)	0.174	
Coefficient K (–)	0.351	
Contact angle θ (deg)	60	
Interaction ratio α (–)	0.5	
Gravity g (m/s^2)	9.8	
Particle spacing l_0 (m)	5.0×10^{-5}	1.0×10^{-4}
Effective radius (viscosity) h_v (m)	1.55×10^{-4}	3.1×10^{-4}
Effective radius (pressure) h_p (m)	1.55×10^{-4}	3.1×10^{-4}
Effective radius (surface tension) h_s (m)	1.75×10^{-4}	3.5×10^{-4}
Time step width Δt (s)	1.0×10^{-6}	2.0×10^{-6}
Maximum Squeeze Reynolds number Re (–)	1.1×10^{-2}	

Fig. 8 Computational model of squeeze film calculation

squeeze motion, in which the two plates approach, the positive pressure is induced, whereas the negative pressure is induced in the negative squeeze motion, in which the two plates separate. The calculation conditions are shown in Table 2, where the experimental study by Kuroda et al. [44, 45] is referred. It should be noted that according to the experiment by Kuroda et al., the frequency of the sinusoidal oscillation is small enough to avoid cavitation onset in the squeeze film, which is left as a future work. In the calculation, the two different particle spacings of $l_0 = 5.0 \times 10^{-5}$ m and 1.0×10^{-4} m were applied to evaluate the influence of the particle resolution. The effective radii h_v and h_p for the viscous and pressure terms were set to be the same as $3.1l_0$, whereas the one for the surface tension model h_s was set to $3.5l_0$. The coefficient a in the surface tension model and the interaction ratio α in the wettability model were set as in Eqs. (16) and (18). The maximum squeeze Reynolds number Re based on the film thickness H and squeeze velocity V is 1.1×10^{-2}.

The computational model of the squeeze film calculation at the initial state is shown in Fig. 8. The oil vessel and moving plate were modeled by wall particles, and four layers of the wall particle were given for each object. The no-slip condition
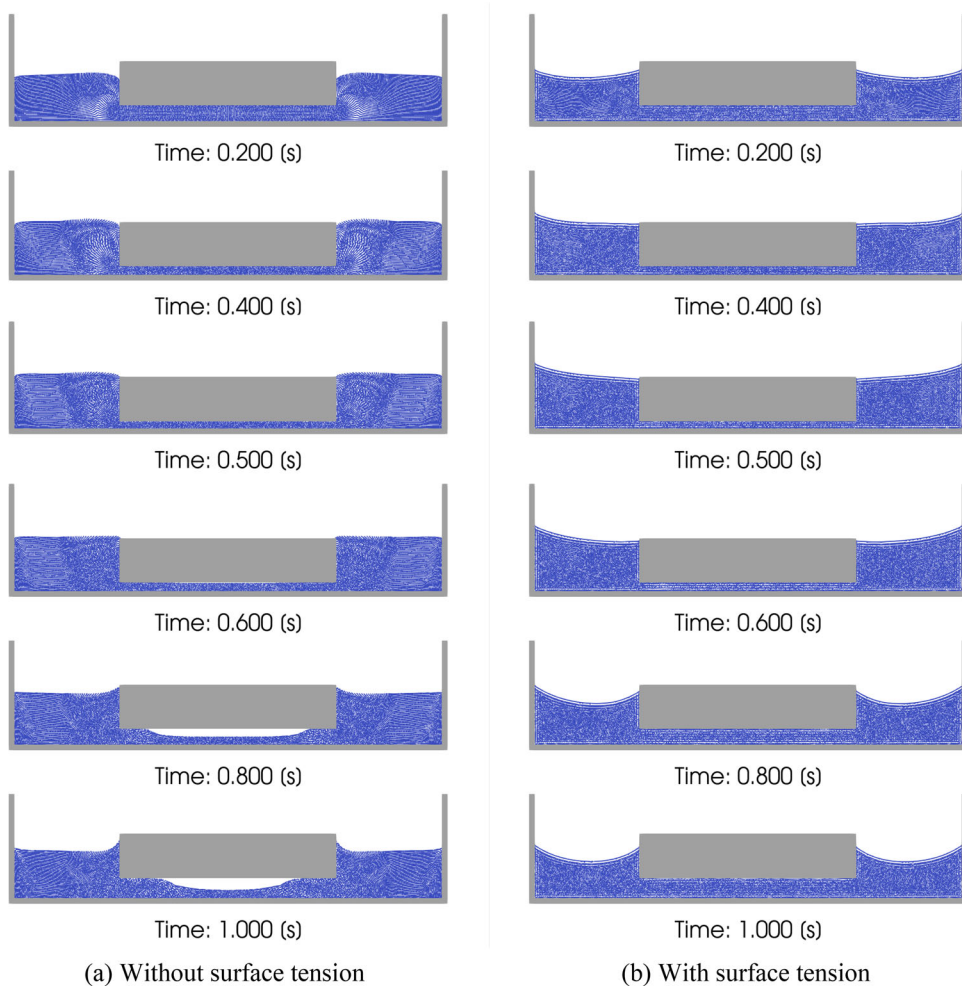
was specified for the wall particles by setting a velocity of zero for the vessel wall particles and the squeeze velocity $V(t)$ (Eq. 32) for the moving plate. The fluid film was modeled by the fluid particle, and the initial film thickness was given as $H_0 = 1.0 \times 10^{-3}$ m. The gravity was given in the vertical direction.

The development of the squeeze film shape for the base case ($l_0 = 5.0 \times 10^{-5}$ m) is shown in Fig. 9. In the positive squeeze phase at $t = 0.2, 0.4, 0.5$ s, in which the moving plate goes down, the result of the case with the surface tension model shows meniscus in the vicinity of the walls due to the wettability model, whereas that of the case without the surface tension model does not. A clear difference between the two cases can be observed in the negative squeeze phase at $t = 0.6, 0.8, 1.0$ s, in which the moving plate goes up. In the case with the surface tension model, the squeeze film is attached to the moving wall and keeps growing by sucking the neighbor fluid near the edge of the squeeze film region. In contrast, in the case without the surface tension model, the squeeze film is detached from the moving plate, and the film thickness does not grow.

The development of pressure in the squeeze film for the base case ($l_0 = 5.0 \times 10^{-5}$ m) is shown in Fig. 10. In the positive squeeze phase at $t = 0.2, 0.4, 0.5$ s, the positive pressure is generated around the center of the film in both cases with and without the surface tension model. A clear difference between the two cases can be observed in the negative squeeze phase at $t = 0.6, 0.8, 1.0$ s. In the case with the surface tension model, the negative pressure can be observed in the squeeze film, whereas the one without the surface tension model cannot be seen. In the case with the surface tension model, the tension is imposed in the squeeze film due to the negative squeeze motion and wettability between the fluid and the moving wall. The tension induces the negative pressure, which plays a role of sucking the neighboring fluid into the squeeze film and keeping the squeeze film attached to the moving plate, i.e., forming the meniscus. Here, it should be noted again that the negative pressure prediction is essential to the meniscus formation. This result demonstrates that the two-potential surface tension model could capture the negative pressure as well as surface tension effect. Besides, in Fig. 10b, the virial pressure (Eq. 27) close to the free surface

Fig. 9 Development of squeeze film shape calculated with $l_0 = 5.0 \times 10^{-5}$ m. **a** Without surface tension and **b** With surface tension

Time: 0.200 (s)

Time: 0.400 (s)

Time: 0.500 (s)

Time: 0.600 (s)

Time: 0.800 (s)

Time: 1.000 (s)

(a) Without surface tension

Time: 0.200 (s)

Time: 0.400 (s)

Time: 0.500 (s)

Time: 0.600 (s)

Time: 0.800 (s)

Time: 1.000 (s)

(b) With surface tension

is always displayed negative because of the tangential tension coming from the two-potential surface tension model [40].

The pressure–time history at the center of the squeeze film ($x = 0$) is shown in Fig. 11. The pressure was evaluated by space averaging the virial pressure (Eq. 27) in the region enclosed by the center circle with its radius of $3.1l_0$. For comparison, the result of the coarse case with the larger particle spacing $l_0 = 1.0 \times 10^{-4}$ m is also plotted. The computed results are compared with the result by the classic Reynolds eq. for the parallel-surface squeeze film of infinite width [43]

$$\frac{d}{dx}\left(\frac{H^3}{\mu}\frac{dp}{dx}\right) = 12V \tag{33}$$

and boundary conditions

$$\frac{dp}{dx}\bigg|_{x=0} = 0 \tag{34}$$

$$p(x_L) = p_a,$$

where H is the squeeze film thickness as a function of time, and p_a is the hydrostatic pressure at the position of x_L, which is the left end of the squeeze film and given as $x_L = -W/2$, as shown in Fig. 6. By integrating Eq. (33) with the boundary condition Eq. (34), the pressure as a function of time t and position x is given as

$$p(t, x) = \frac{6\mu V(t)}{H(t)^3}\left(x^2 - \frac{W^2}{4}\right) + p_a. \tag{35}$$

Here, p_a can be negligible ($p_a = 0$ Pa) because the oil height is very low. As shown in Fig. 11, the computed result in the base case with the surface tension model predicts the analytical solution well (Eq. 35). However, the one in the coarse case slightly underpredicts the maximum and minimum pressure due to insufficient particle resolution. The computed result without the surface tension model predicts the positive pressure history from $t = 0$ to 0.5 s. In contrast, it fails to predict the negative pressure history because of the lack of tension in the squeeze film from $t = 0.5$ to 1.0 s, as shown in Fig. 10.

Fig. 10 Development of pressure in squeeze film calculated with $l_0 = 5.0 \times 10^{-5}$ m. **a** Without surface tension and **b** With surface tension


(a) Without surface tension

(b) With surface tension
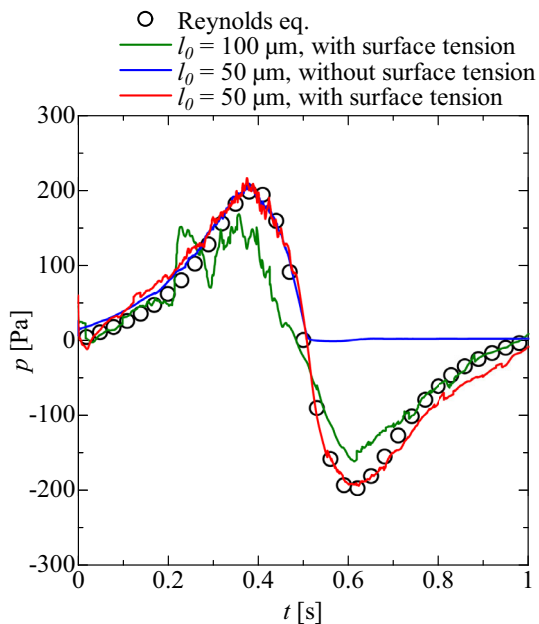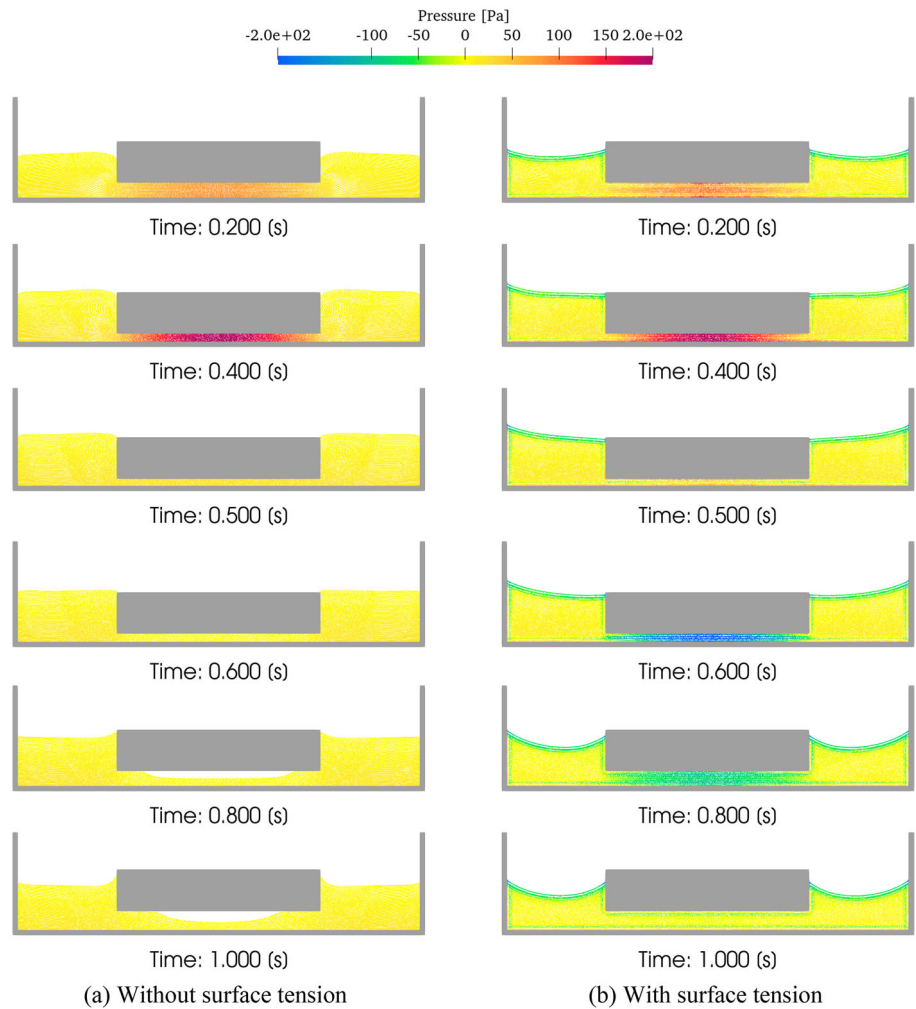
Fig. 11 Pressure–time history at center of squeeze film

The pressure profiles in the horizontal direction at $t = 0.4$ and 0.6 s are shown in Fig. 12. The pressure was also evaluated by space averaging the virial pressure (Eq. 27) in control volumes with the length of $3.1l_0$ between the bottom and moving walls. As can be seen in Fig. 12, the computed results in the base case ($l_0 = 5.0 \times 10^{-5}$ m) almost agree well with the analytical solutions (Eq. 35). However, some fluctuation can be observed, possibly because of the non-uniform particle distributions in the film. Overall, the result in the coarse case ($l_0 = 5.0 \times 10^{-5}$ m) underestimated the pressure profiles due to insufficient particle resolution. As a result, it is confirmed that the squeeze film effect can also be predicted quantitatively by the MPH-I method with the two-potential (CPP and DGP) surface tension model.

4 Conclusions

In this study, a physically consistent particle method, the Moving Particle Hydrodynamics (MPH) method [36–40],

Fig. 12 Pressure distribution in squeeze film. **a** $t = 0.4$ s and **b** $t = 0.6$ s

(a) $t = 0.4$ s

(b) $t = 0.6$ s
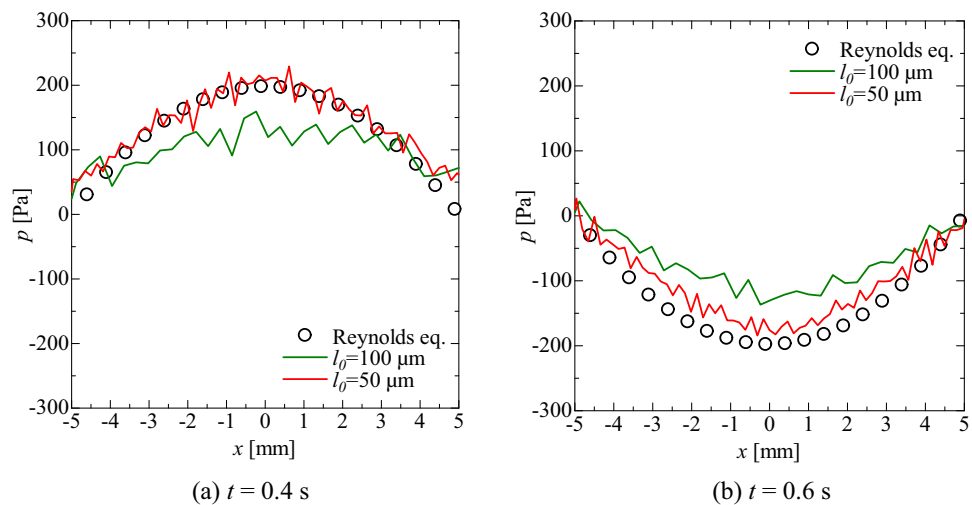
was applied to the fundamental fluid film lubrication problems. To avoid the time step size restriction due to the small length scale and the high viscosity in the lubrication problems, the incompressible MPH (MPH-I) method with the pressure substituting implicit solver [39] was employed with the two-potential (cohesive pressure and density gradient potentials) surface tension model [40]. For the validation in specific, the problems with respect to the wedge film and squeeze film effects, which are the fundamental pressure generation mechanisms in the fluid film lubrication, were calculated.

In the wedge film calculation, the steady-state pressure profile in the film agreed well with the experiment [41]. The positive pressure due to the wedge film effect and the negative pressure in the exit meniscus owing to the divergent flow passage, the sliding velocity, and the wettability were well reproduced in the calculation. In the squeeze film calculation, the unsteady pressure–time history at the center of the squeeze film, including the negative pressure, agreed well with the analytical solution obtained by the classic Reynolds equation for the parallel-surface squeeze film of infinite width [43]. The pressure profiles in the horizontal direction at the time of the maximum and minimum pressure were also well reproduced. In the two cases, the employed method exhibited high accuracy and robustness for the fundamental fluid film lubrication problems even with the negative pressure. Overall, it was confirmed that the employed method is promising for predicting the fluid film lubrication problems.

Declarations

References

1. Lucy LB (1977) A numerical approach to the testing of the fission hypothesis. Astron J 82:1013–1024. https://doi.org/10.1086/112164

2. Gingold RA, Monaghan JJ (1977) Smoothed particle hydrodynamics: theory and application to non-spherical stars. Mon Not R Astron Soc 181(3):375–389. https://doi.org/10.1093/mnras/181.3.375

3. Koshizuka S, Oka Y (1996) Moving particle semi-implicit method for fragmentation of incompressible fluid. Nucl Sci Eng 123(3):421–434. https://doi.org/10.13182/NSE96-A24205

4. Koshizuka S (2011) Current achievements and future perspectives on particle simulation technologies for fluid dynamics and heat transfer. J Nucl Sci Technol 48(2):155–168. https://doi.org/10.1080/18811248.2011.9711690

5. Gotoh H, Khayyer A (2016) Current achievements and future perspectives for projection-based particle methods with applications in ocean engineering. J Ocean Eng Mar Energy 2:251–278. https://doi.org/10.1007/s40722-016-0049-3

6. Violeau D, Rogers BD (2016) Smoothed particle hydrodynamics (SPH) for free-surface flows: past, present and future. J Hydraul Res 54(1):1–26. https://doi.org/10.1080/00221686.2015.1119209

7. Koshizuka S, Shibata K, Kondo M, Matsunaga T (2018) Moving particle semi-implicit method: a meshfree particle method for fluid dynamics. Academic Press

8. Ye T, Pan D, Huang C, Liu M (2019) Smoothed particle hydrodynamics (SPH) for complex fluid flows: recent developments in methodology and applications. Phys Fluid 31:011301. https://doi.org/10.1063/1.5068697

9. Li G, Gao J, Wen P, Zhao Q, Wang J, Yan J, Yamaji A (2020) A review on MPS method developments and applications in nuclear engineering. Comput Methods Appl Mech Eng 367:113166. https://doi.org/10.1016/j.cma.2020.113166

10. Ji Z, Stanic M, Hartono EA, Chernoray V (2018) Numerical simulations of oil flow inside a gearbox by smoothed particle hydrodynamics (SPH) method. Tribol Int 127:47–58. https://doi.org/10.1016/j.triboint.2018.05.034

11. Muto K, Sakai I, Ozaki N (2010) Calculation of stirring resistance of fluid using particle method. Trans Soc Autom Eng Jpn 41(1):147–151. https://doi.org/10.11351/jsaeronbun.41.147

12. Yuhashi N, Matsuda I, Koshizuka S (2016) Calculation and validation of stirring resistance in cam-shaft rotation using the moving particle semi-implicit method. J Fluid Sci Technol 11(3):JFST0018. https://doi.org/10.1299/jfst.2016jfst0018

13. Yuhashi N, Koshizuka S (2020) Calculation of oil churning in crankcase of reciprocating pump (calculation of free surface flow by moving particle semi-implicit method). Trans JSME 86(881):1900343. https://doi.org/10.1299/transjsme.19-00343

14. Kyle JP, Terrell EJ (2013) Application of smoothed particle hydrodynamics to full-film lubrication. ASME J Tribol 135(4):041705. https://doi.org/10.1115/1.4024708

15. Tanaka K, Fujino T, Fillot N, Vergne P, Iwamoto K (2019) Numerical simulation of hydrodynamic lubrication by SPH method. Abstract Book of 46th Leeds-Lyon Symposium on Tribology 21

16. Brackbill JU, Kothe DB, Zemach C (1992) A continuum method for modeling surface tension. J Comput Phys 100(2):335–354. https://doi.org/10.1016/0021-9991(92)90240-Y

17. Khayyer A, Gotoh H, Shimizu Y (2017) Comparative study on accuracy and conservation properties of two particle regularization schemes and proposal of an optimized particle shifting scheme in ISPH context. J Comput Phys 332:236–256. https://doi.org/10.1016/j.jcp.2016.12.005

18. Paggi M, Amicarelli A, Lenarda P (2021) SPH modelling of hydrodynamic lubrication: laminar fluid flow-structure interaction with no-slip conditions for slider bearings. Comput Part Mech 8:665–679. https://doi.org/10.1007/s40571-020-00362-1

19. Negishi H, Fujihara H, Takahashi H, Shibata K, Maniwa K, Obara S (2020) Numerical analysis of fluid lubrication in line contact by using the MPS method. Trans JSME 86(890):2000241. https://doi.org/10.1299/transjsme.20-00241

20. Yamada D, Imatani T, Shibata K, Maniwa K, Obara S, Negishi H (2022) Application of improved multiresolution technique for the MPS method to fluid lubrication. Comput Part Mech 9:421–441. https://doi.org/10.1007/s40571-021-00420-2

21. Shibata K, Koshizuka S, Matsunaga T, Masaie I (2017) The overlapping particle technique for multi-resolution simulation of particle methods. Comput Methods Appl Mech Eng 325:434–462. https://doi.org/10.1016/j.cma.2017.06.030

22. Dowson D, Taylor CM (1979) Cavitation in bearings. Annu Rev Fluid Mech 11:35–65. https://doi.org/10.1146/annurev.fl.11.010179.000343

23. Swegle JW, Hicks DL, Attaway SW (1995) Smoothed particle hydrodynamics stability analysis. J Comput Phys 116(1):123–134. https://doi.org/10.1006/jcph.1995.1010

24. Monaghan JJ (2000) SPH without a tensile instability. J Comput Phys 159(2):290–311. https://doi.org/10.1006/jcph.2000.6439

25. Dyka CT, Randles PW, Ingel RP (1997) Stress points for tension instability in SPH. Int J Numer Meth Eng 40(13):2325–2341. https://doi.org/10.1002/(SICI)1097-0207(19970715)40:13%3c2325::AID-NME161%3e3.0.CO;2-8

26. Belytschko T, Xiao S (2002) Stability analysis of particle methods with corrected derivatives. Comput Math Appl 43:329–350. https://doi.org/10.1016/S0898-1221(01)00290-5

27. Hicks DL, Liebrock LM (2004) Conservative smoothing with B-splines stabilizes SPH material dynamics in both tension and compression. Appl Math Comput 150(1):213–234. https://doi.org/10.1016/S0096-3003(03)00222-4

28. Dilts GA (1999) Moving-least-squares-particle hydrodynamics: consistency and stability. Int J Numer Methods Eng 44(8):1115–1155. https://doi.org/10.1002/(SICI)1097-0207(19990320)44:8%3c1115::AID-NME547%3e3.0.CO;2-L

29. Xu R, Stansby P, Laurence D (2009) Accuracy and stability in incompressible SPH (ISPH) based on the projection method and a new approach. J Comput Phys 228(18):6703–6725. https://doi.org/10.1016/j.jcp.2009.05.032

30. Koshizuka S, Nobe A, Oka Y (1998) Numerical analysis of breaking waves using the moving particle semi-implicit method. Int J Numer Methods Fluids 26(7):751–769. https://doi.org/10.1002/(SICI)1097-0363(19980415)26:7%3c751::AID-FLD671%3e3.0.CO;2-C

31. Khayyer A, Gotoh H (2008) Development of CMPS method for accurate water-surface tracking in breaking waves. Coast Eng J 50(2):179–207. https://doi.org/10.1142/S0578563408001788

32. Khayyer A, Gotoh H (2011) Enhancement of stability and accuracy of the moving particle semi-implicit method. J Comput Phys 230(8):3093–3118. https://doi.org/10.1016/j.jcp.2011.01.009

33. Tsuruta N, Khayyer A, Gotoh H (2013) A short note on dynamic stabilization of moving-particle semi-implicit method. Comput Fluids 82:158–164. https://doi.org/10.1016/j.compfluid.2013.05.001

34. Lee BH, Park JC, Kim MH, Hwang SC (2011) Step-by-step improvement of MPS method in simulating violent free-surface motions and impact-loads. Comput Methods Appl Mech Eng 200:1113–1125. https://doi.org/10.1016/j.cma.2010.12.001

35. Matsunaga T, Koshizuka S (2022) Stabilized LSMPS method for complex free-surface flow simulation. Comput Methods Appl Mech Eng 389:114416. https://doi.org/10.1016/j.cma.2021.114416

36. Kondo M (2021) A physically consistent particle method for incompressible fluid flow calculation. Comput Part Mech 8:69–86. https://doi.org/10.1007/s40571-020-00313-w

37. Kondo M, Fujiwara T, Masaie I, Matsumoto J (2022) A physically consistent particle method for high-viscous free-surface flow calculation. Comput Part Mech 9:265–276. https://doi.org/10.1007/s40571-021-00408-y

38. Kondo M, Matsumoto J (2021) Weakly compressible particle method with physical consistency for spatially discretized system. Trans JSCES 2021:20210006. https://doi.org/10.11421/jsces.2021.20210006

39. Kondo M, Matsumoto J (2021) Pressure substituting implicit solver to speed-up moving particle hydrodynamics method for high-viscous incompressible flows. Trans JSCES 2021:20210016. https://doi.org/10.11421/jsces.2021.20210016

40. Kondo M, Matsumoto J (2021) Surface tension and wettability calculation using density gradient potential in a physically consistent particle method. Comput Methods Appl Mech Eng 385:114072. https://doi.org/10.1016/j.cma.2021.114072

41. Floberg L (1965) On hydrodynamic lubrication with special reference to sub-cavity pressures and number of streamers in cavitation regions. Acta Poly Scand Mech Eng Ser 19:3–35

42. Bruyere V, Fillot N, Morales-Espejel GE, Vergne P (2012) A two-phase flow approach for the outlet of lubricated line contacts. ASME J Tribol 134(4):041503

43. Hamrock BJ, Schmid SR, Jacobson BO (2004) Fundamentals of fluid film lubrication, 2nd edn. CRC Press
44. Hori Y (2016) Hydrodynamic lubrication. Springer
45. Kuroda S, Hori Y (1978) An experimental study on cavitation and tensile stress in a squeeze film. Lubrication 23:436–442 (**in Japanese**)
46. Goldstein H, Safko JL, Poole CP (2013) Classical mechanics. Pearson New International Edition
47. Monaghan JJ (1992) Smoothed particle hydrodynamics. Ann Rev Astron Astrophys 30:543–574. https://doi.org/10.1146/annurev.aa.30.090192.002551
48. Hu XY, Adams NA (2006) Angular-momentum conservative smoothed particle dynamics for incompressible viscous flows. Phys Fluids 18:101702. https://doi.org/10.1063/1.2359741
49. Nishida A (2010) Experience in developing an open source scalable software infrastructure in Japan. Computer science and its applications-ICCSA 2010, Lecture Notes in Computer Science, Springer, pp. 448–462
50. https://www.ssisc.org/lis/index.en.html
51. Gray CG, Gubbins KE (1984) Theory of molecular fluids: fundamentals. Oxford University Press